A Simulation Experiment on In-Situ Observation of Short-Wavelength Scale Dynamic Processes and Potential Applications to Wide-Swath Interferometric Altimetry Validation

Chen Wang, Fangjie Yu , Zhiyuan Zhuang, Junwu Tang, Hanwei Sun, and Ge Chen

Abstract—**Short-wavelength (15–150 km) ocean phenomena are difficult to be observed by conventional altimeter due to the sampling method limited the resolution of the data. It is, therefore, the future wide-swath interferometric altimetry (WIA) missions like "SWOT" and "Guanlan" are designed to observe these phenomena. However, observing the short-wavelength dynamic process of the high eddy kinetic energy (EKE) region is still a challenge. The short-wavelength validation of WIA is also an urgent problem to be solved. In-situ observation platforms array can provide data set with high spatial and temporal resolution, which can capture short-wavelength dynamic process and validate the altimeter data. Simulation is a key to verify the feasibility of the observation strategy. In this article, we carried out simulated observation experiments based on high spatial-temporal resolution numerical models and introduced motion model of mooring and keep-station glider to improve the accuracy of in-situ observation simulation under the influence of the dynamic ocean currents which optimized by deep learning methods. In this experiment, the steric height, reconstructed by different observation array strategies, and the sea surface height of the measured positions are compared based on wavenumber spectrum. We tested the performance of the mooring array, station-keeping glider array, mooring and wave-energy profiling buoy (M&WPB) combination array, and multidevice array. The results show that the glider and M&WPB arrays have better performance of strong current regions. It could be helpful for the observation of dynamic processes in high EKE regions and has potential application for the validation of WIA.**

Chen Wang and Zhiyuan Zhuang are with the College of Marine Technology, Faculty of Information Science and Engineering, Ocean University of China, Qingdao 266100, China (e-mail: wangschen2408@stu.ouc.edu.cn; zhuangzhiyuan@stu.ouc.edu.cn).

Fangjie Yu and Ge Chen are with the College of Marine Technology, Faculty of Information Science and Engineering, Ocean University of China, Qingdao 266100, China, and also with the Laboratory for Regional Oceanography and Numerical Modeling, Qingdao National Laboratory for Marine Science and Technology, Qingdao 266237, China (e-mail: yufangjie@ouc.edu.cn; gechen@ouc.edu.cn).

Junwu Tang is with the Pilot National Laboratory for Marine Science and Technology (Qingdao), Qingdao 266237, China (e-mail: jwtang@qnlm.ac).

Hanwei Sun is with the Beijing Institute of Radio Measurement, Beijing 100143, China (e-mail: sunhw12@tsinghua.org.cn).

Digital Object Identifier 10.1109/JSTARS.2021.3119034

Index Terms—**Altimetry, marine equipment, simulation.**

I. INTRODUCTION

OCEANIC processes of short-wavelength range (15–150 km) crucially affecting the ocean physics and ecology up to the climate scale, because of the strong gradients in ocean properties created by their energetic dynamics [1]. However, the one-dimensional profiles sea surface height (SSH) data onto conventional altimeter cannot capture dynamic process below 150 km wavelength scale due to the limitation of resolution [2]. Wide-swath interferometric altimetry (WIA), as the developing direction of future oceanographic satellites, has broken through the resolution limitation that conventional altimeter can only observe oceanographic phenomena in mesoscale or greater (150–1000 km wavelength) [3]. The Tiangong-2 [4] and soon-to-be-launched "Surface Water Ocean Topography (SWOT) Mission" [5], "Guanlan" [6] and other possible missions will provide high-precision two-dimensional (2-D) SSH data as the basis of the study of short-wavelength scale dynamic processes. Nevertheless, the simulation showed that more than one-third of eddies cannot be observed by SWOT in the high eddy kinetic energy (EKE) region (the Kuroshio Extension), even without considering the effect of internal tides [7]. Meanwhile, with the development of altimeter technology, the validation methods for conventional altimeters no longer meet the needs of many future altimeter missions, especially the validation requirements for WIA 2D data areas [8], [9].

In-situ observation may be the solution to these problems. It can provide surface and subsurface data with high spatial and temporal resolution as the complementary data sets [10] for altimeter as well as independently used in various fields of oceanic research [11]–[14], including the study of ocean dynamic processes and the validation of satellite data. The three-dimensional structure of a mesoscale eddy in the Kuroshio extension region is observed by combining the acoustic Doppler current profiler (ADCP) data with satellite altimeter data [15]. The in-situ observation array could be used in oceanic study effectively through the coordination of multiple devices. The Kuroshio extension system study quantified processes governing the variability of and the interaction between the Kuroshio extension and the recirculation gyre with the array of 43 inverted

echo sounders equipped [16]. And a device called "CalNaGeo" is designed that arranges multiple GNSS sensors in a network and drags them behind the ship, which can be used to observe the 2-D SSH in a small area and validate the data of the wide-swath area of WIA [17]. Zhang *et al.* [18] verified the consistency between the SH obtained from the observation of Argo profile conductivity-salinity depth (CTD) data and the SSH data on altimeter along-track. Nevertheless, few studies focus on the observation in short-wavelength scale with real trial data. Simulation is a key to verify the feasibility of the observation strategy and provide guidance for real sea trials to avoid the loss of unpredictable results. An observing system simulation experiment is designed to evaluate the practicability of SWOT validation by various in-situ single-equipment arrays including instrumented moorings, underwater gliders, underway conductivity–temperature depth (UCTD) sensors, and pressure-sensor equipped inverted echo sounders (PIES) [19]. The results showed that the mooring observation array could meet the requirements of the mission and the station-keeping glider observation array have high potential. Both experiment sites were located in the low EKE region with low flow velocity. However, the in-situ observation equipment will be affected by the sea conditions during the period of observation, especially the current, which makes the sensor unable to collect corresponding data in the preset position [20]. Thus, accurately simulating the sampling state of the observation equipment under the ocean currents is particularly important to the study [21]–[23].

The future use of WIA will allow us to understand the submesoscale phenomena better. However, validation and observation are difficult in places where submesoscale phenomena are active and real sea trials are costly. It is important to formulate and verify the strategy in advance. In this article, we carried out a simulated in-situ observation experiment at the intersection of three eddies in the Kuroshio extension, using different equipment for networking observation, and tried to use multidevice joint networking to improve the observation effect. We introduced the motion model of mooring and keep-station glider affected by currents based on deep learning method respectively to improve the accuracy of simulation observation. Based on wavenumber spectrum analysis, we compared the SSH at the corresponding point in the model data with the steric height(SH) obtained by simulation and compared the pros and cons of different network strategies for observation and validation. We introduce data and methods in Section II, results in Section III, and conclusion and discussion in Section IV.

II. DATA AND METHODS

A. Data

1) Numerical Model: The numerical model we used is a virtual ocean, and its scientificity and time-spatial resolution determine the quality of the experiment. The in-situ observation simulation experiment is based on the Regional Ocean Modeling System (ROMS) [24] provided by Pilot National Laboratory for Marine Science and Technology (Qingdao), Qingdao, China [25]. The ROMS is configured in the Kuroshio Extension area [$146.6° − 168.5°$ E and $29° − 42.6°$ N, as shown in the yellow
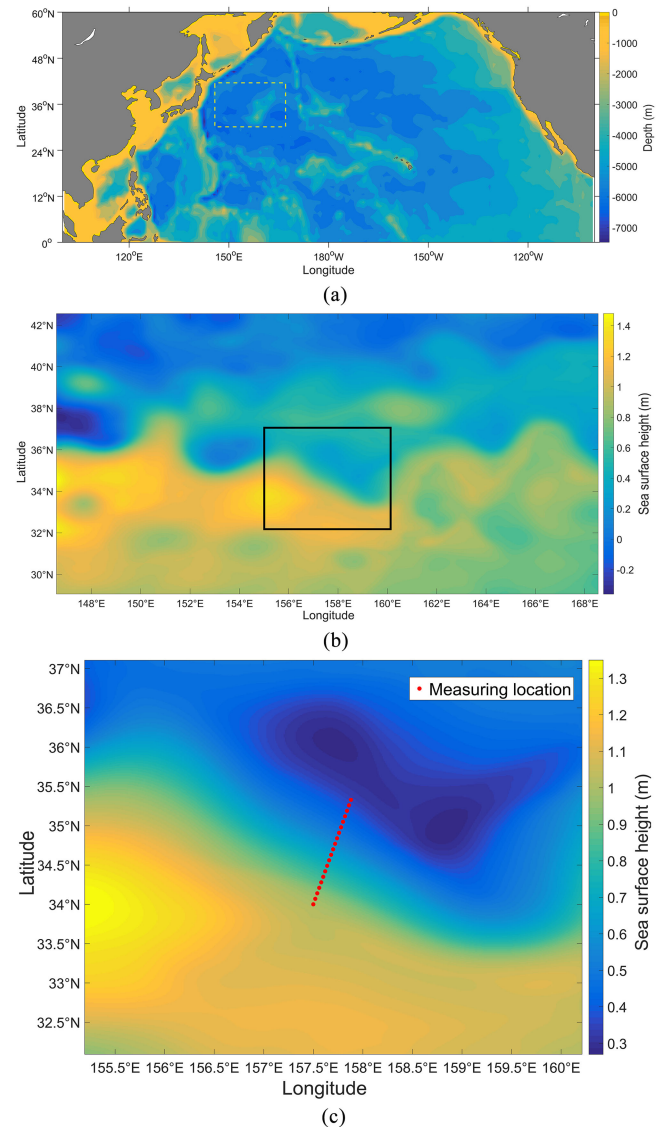

Fig. 1. Snapshots of the SSH field in the (b) 1-km ROMS simulations on 15 October 2004 and the area is shown in (a) yellow dash box. (c) is a zooming snapshot of the black box in (b), three adjacent mesoscale vortices can be seen. The red points at the location of measuring points.

dash box in Fig. 1(a)] where the dynamic process was active from September 30, 2004 to March 31, 2005. The high EKE of the study area enables us to test the observation capability of various field observation equipment under harsh sea conditions. The simulation has a horizontal resolution of 1 km, a time resolution of 3 h, and 65 levels in a vertical terrain-following coordinate. The vertical grid size of the upper 100 m is 4.7–6.0–m. Momentum uses a biharmonic horizontal Smagorinsky-like mixing scheme [26] and vertical mixing uses a K-profile parameterized (KPP) turbulent mixing closed scheme [27]. No horizontal mixing parameterization is applied to the tracer.

In this article, we use the data from October 1, 2004, to conduct a 30-day simulation experiment in the area where three mesoscale eddies intersect and submesoscale phenomena are frequent [as shown in Fig. 1(b) and (c)] to test the differences of different observation-network strategies.

2) Mooring Dataset: The dataset we used to train and test the mooring motion model was collected by three moorings anchored from November 2017 to May 2018 at the Kuroshio Extension region. The CTDs are used to collect position data, the ACMs (1500 m-full depth) and ADCP (0–1500 m) of moorings are ocean current meters applied to acquire current data.

3) Glider Dataset: The dataset we used to train the glider motion model was collected by sea-wing gliders from two ocean observation experiments (from April 28, 2015 to June 1, 2015, and from July 3, 2016 to July 16, 2016), where the investigation areas are located in the northern South China Sea.

B. In-Situ Observation Equipment Simulation

The simulation of equipment is the core of the in-situ observation simulation experiment. In this article, we choose instrumented ocean mooring and station-keeping underwater glider, which can validate the WIA data [19]. Moreover, WPB that could encrypt sampling of the upper 200 m ocean was added as a supplement. Gradient descent algorithm was used to predict the trajectory of mooring and glider under the influence of currents, the motion models were generated and applied in the experiments.

1) Instrumented Ocean Mooring: Instrumented ocean mooring is the most commonly used in-situ observation equipment in oceanographic research in the deep sea. It is the gold standard for fixed location in-situ measurement of the ocean [23]. However, because of the sea conditions, especially the influence of the currents, the mooring will have a sinking (bias) effect. Thus, the upper ocean sampling data will be missing. It is very important to establish a model to simulate the extent to which the equipment is affected by the flow velocity and to evaluate it [21], [22].

In this article, we constructed a gradient descent algorithm for instrumented ocean mooring movement, and its objective function can be expressed as

$$J\left(\theta_0, \theta_1\right) = \frac{1}{2m} \sum_1^m \left(h_\theta\left(x^{(i)}\right) - y^{(i)} \right)^2. \quad (1)$$

Partial derivative of objective function

$$\frac{\Delta J\left(\theta_0, \theta_1\right)}{\Delta \theta_j} = \frac{1}{m} \sum_1^m \left(h_\theta\left(x^{(i)}\right) - y^{(i)} \right) x_j^{(i)} \quad (2)$$

where $h_\theta(x(i))$ is the fitting function, which is the point product of the input data and the parameters, expressed as the displacement we predicted; m is the number of data in the data set; 1/2 is a constant, and the partial derivative is calculated when implemented cancellation eliminate excess constant coefficient; x is the input data, y represents the amount of displacement input; $i = 11 +$ batch size, $1 +$ bitch size $+$ batch size …… shows a sample divided by the batch size, and j represents a number of features.

Iteratively update the parameters

$$\theta_j := \theta_j - \alpha \frac{1}{\text{batch size}} \sum_{k=i}^{i+9} \left(h_\theta\left(x^{(k)}\right) - y^{(k)} \right) X_j^{(k)} \quad (3)$$

where α represents the set learning rate.

According to the parameter values calculated by using gradient descent algorithm and related data, we construct the motion model of each depth layer of the mooring. Substituting the flow
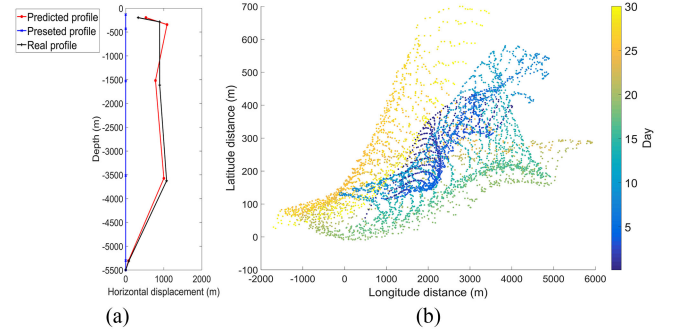

Fig. 2. (a) Comparison between the preset profile (blue), real profile (black), and the predicted profile (red) using the mooring movement model, points with different shapes are the positions of CTDs. (b) is the deviation of the surfacing positions of 20 gliders for 30 d.

TABLE I
RANDOM ERRORS OF IN-SITU OBSERVATION PLATFORMS

In-situ Observation Platforms	Temperature(ºC)	Conductivity(psu)
Mooring	±0.01	±0.02
Glider	±0.01	±0.01
Wave-energy profiling buoy	±0.002	±0.003

velocity data corresponding to the predicted time into the mooring movement model, calculating the movement displacement of each layer of the mooring, the movement trajectory could be obtained at the flow velocity. We compared the predicted trajectories with the real data of CTD locations and found that the trajectories fit well, as shown in Fig. 2(a).

The measurement noise of the CTDs is represented by a Gaussian random process. We assumed that the random errors of the CTD instrument as shown in Table I. The random errors for sampling every 5-min take various factors into account that may be encountered that affect the sensor accuracy, higher than many CTD designs. Meanwhile, because of the time resolution of ROMS, the noise amplitude is scaled by $\sqrt{1/36}$ (36 times sampling every 3 h). The sampled data are interpolated by the numerical model in three dimensions as same as other simulated observation platforms.

2) Station-Keeping Glider: As an autonomous underwater vehicle (AUV), glider has gradually become a reliable tool for data collection and has been widely used in marine research [28]. Compared with mooring, underwater gliders have the characteristics of low cost and relatively easy deployment. And with the continuous development of control technology, the station keeping glider can be used as a virtual mooring. A glider with excellent performance, such as the Slocum [29], could be equipped with a propeller and supplemented by a suitable station-keeping algorithm. Long-term profile observation of the upper ocean (500 m) can control the observation range within 1 km of the set point [23].

Under the numerical model resolution conditions (horizontal resolution: 1 km; time resolution: 3 h), We simply use the existing glider surfacing position data and the space-time matching AVISO velocity data product to train the glider motion parameters affected by current velocity based on gradient descent
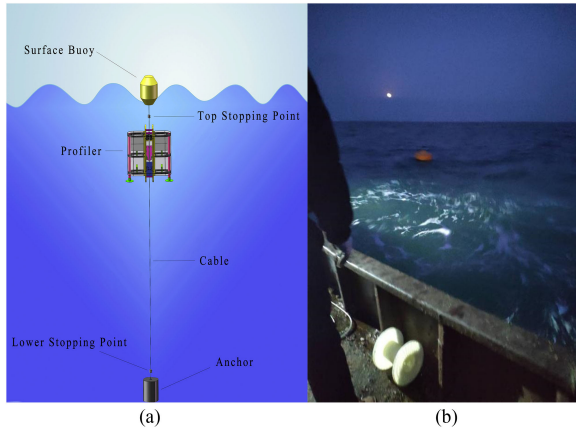
Fig. 3.   (a) Schematic diagram of the wave-energy profiling buoy and (b) the photo of wave-energy profiling buoy when it working.

algorithm and give the glider a horizontal velocity to the set point after the first surfacing.

We are benchmarking the best performance of the glider at this stage, presetting depth of 2000 m and vertical speed of 0.2 m/s, with a V-shaped dive (two profiles) less than 6 h. The diving angle of the device is not set and the horizontal speed is determined by the glider motion parameters, which are affected by the current velocity. The vertical sampling rate is set to sampling once per 25 s (5 m). According to the equipment performance, the random errors of the equipment [30] are shown in Table I. Fig. 2(b) shows the deviation of the surfacing positions of 20 gliders for 30 d.

3) Wave-Energy Profiling Buoy: Wave-energy profiling buoy (WPB) is a buoy independently developed by the Marine Information Technology Laboratory of the Ocean University of China that uses wave kinetic energy to collect profile data in the upper ocean. It can collect long-term effective profile data at a single point. The three-stage structure includes a surface buoy at the top, a profiler in the middle, and an anchor at the bottom. Cables are used to connect the three parts. With the ups and downs of the waves, the profiler will slide between upper and lower restricted positions. At the same time, a special mechanical core component is designed in the profiler to ensure that the vertical movement of the profiler is monotonous. In this process, the CTD sensor will sample data to obtain high-resolution profile temperature, depth, conductivity, and other parameter data. The schematic diagram of the equipment is shown in Fig. 3.

The sampling depth of the equipment can reach 200 m. The descending depends on the wave generated by the wind to provide power. After reaching the lower stopping point, it ascends at a speed of about 0.4 m/s relies on buoyancy.

In this simulation observation experiment, the sampling depth is set to 200 m, and the vertical sampling rate is set to every 1 m. According to the equipment performance, the random errors of the sensor are shown in Table I.

C. Steric Height

The steric method, which uses SH reconstructed from the temperature and salt profile data observed by the in-situ observation equipment to validate the SSH, is a commonly used method of validation [18]. SH is the height variety between the isobaric

surface and the geopotential surface due to changes in density of seawater. The isobaric surface (ϕ) can be expressed as

$$\phi = \int_0^z g dz \tag{4}$$

where g is the acceleration due to gravity on Earth. The theoretical basis for using SH to validate SSH can be derived from the following hydrostatic equation:

$$\frac{\partial p}{\partial z} = -\rho g \tag{5}$$

where p represents the pressure, ρ represents the density that can be decomposed as

$$\rho = \rho_0 + \rho' \tag{6}$$

where ρ_0 is the reference potential density (1027.5 kg/m3), ρ' is the potential density anomaly. Equation (5) can also be expressed in the form

$$p_A - p_B = -\rho_0 g (\zeta + h) - \int_{-h}^{\zeta} \rho' g dz. \tag{7}$$

In this equation, p_A refers to the atmospheric surface pressure, p_B refers to the bottom pressure of ocean, ζ is the SSH referenced to z = 0, and -h is the depth of the ocean. Transforming the above formula as

$$\zeta = \frac{p'_B}{\rho_0 g} - \frac{P_A}{\rho_0 g} - \int_{-h}^{0} \frac{\rho'}{\rho_0} dz. \tag{8}$$

In the (8), $p'_B = p_B - \rho_0 g(\zeta + n)$ represents the bottom pressure anomaly. Because of $\zeta \ll h$, the term of $\int_0^\zeta \frac{\rho'}{\rho_0} dz$ could be neglected. In this article, ζ is the SSH which is calculated from ROMS. To calculate geostrophic currents, oceanographers use a modified form of the hydrostatic equation. The vertical pressure gradient (1) can be expressed as

$$\frac{\delta p}{\rho} = \alpha \delta p = -g \delta z = \delta \phi \tag{9}$$

where α refers to specific volume, the value is the reciprocal of density, and the unit of SH is meter (SH = ϕ/g). Therefore, SH can be expressed as

$$SH = \frac{1}{g} \int_{p_B}^{p_A} \alpha (35,0,p) \, dp + \frac{1}{g} \int_{p_B}^{p_A} \alpha' dp = \int_{-h}^{0} \frac{\rho'}{\rho_0} dz \tag{10}$$

where $\alpha (35,0,p)$ are the specific volume of seawater with the salinity of 35 psu, the temperature of 0 °C, and pressure of p. Comparing (8) and (10), it can be seen that the variety of SSH is mainly composed of three parts: sea surface atmospheric pressure, bottom pressure and SH. In this article, the SSH scale within the WIA swath range to be validated is within 150 km wavelengths. Under this scale, the sea level change is mainly dominated by baroclinic pressure [31]. Therefore, theoretically, it is feasible to use SH to validate 2-D SSH within 150 km wavelength scale.

D. Strategy of In-Situ Observation Array

In order to observe short-wavelength (15–150 km) phenomena, we placed 20 devices at intervals of 7.5 km as the inclination angle of the "Guanlan" ascending orbit (as shown in Fig. 1c).
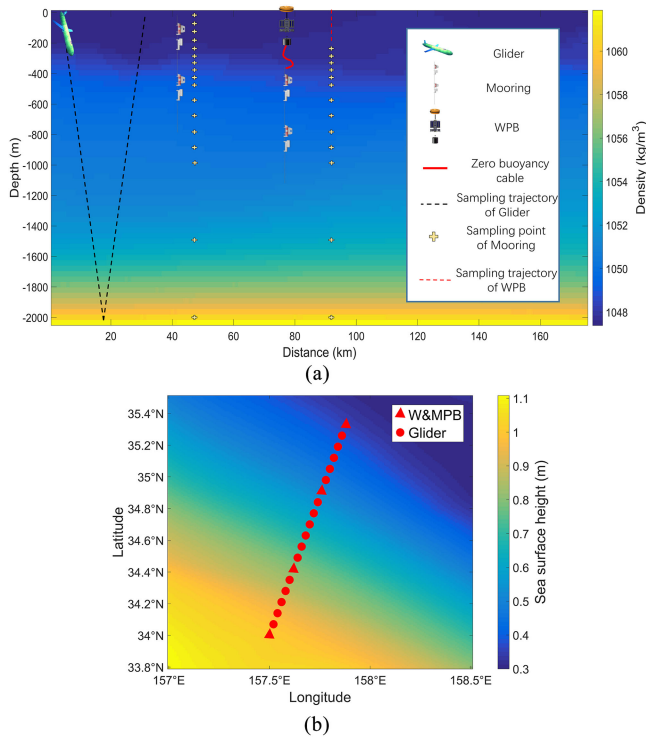
Fig. 4. (a) Sampling diagram of each device. (b) Schematic diagram of multitype devices networking.

Based on the Nyquist sampling theory [32], the minimum scale that observation equipment can observe with 7.5 km interval is 15 km, while 7.5 km∗20 devices can observe 150 km scale. In addition to single-device networking, we explored the possibility of multidevice networking for validation.

1) Single-Type Devices Array: Single-type devices networking includes moorings array and gliders array. The in-situ observation platforms are placed on the observation point according to the above-mentioned rules.

The depth of the mooring CTDs is configured as dense at the top and sparse at the bottom after trial and verification, the detailed process in the result section. The specific configuration strategy is:

Set one every fifty meters for upper 500 m, one every one hundred meters for 500–1000 m, and set one at 1200, 1500, and 2000 m for depths above one thousand meters.

The schematic diagram of equipment sampling is shown in Fig. 4(a).

2) Multitype Devices Array: Different in-situ observation platforms have their advantages and disadvantages. For example, mooring has high-frequency sampling capabilities and a stronger horizontal position retention capability relative to the glider (horizontal offset can be ignored). However, moorings are affected by the current, the deviation will lead to the lack of sampling of the upper ocean, and the cost of moorings is very high. Gliders have the ability of full-depth encrypted sampling, but the sampling time of a profile is too long, and the capture of high-frequency phenomena will be missing. Although the existing technology can control the sampling range of the station-keeping gliders in a smaller area, the horizontal offset

is still large relative to moorings. Therefore, we designed a simulation experiment of multidevice networking to observe the effect.

a) M&WPB

In order to compensate for the lack of sampling of the upper ocean, we added the WPB that can intensively observe the upper 200 m of the ocean beside mooring [Fig. 4(a)]. We connecting the two devices with a 300 m long zero buoyancy cable, and the CTDs of mooring are setting from 250 m depth. A M&WPB as a group, and 20 groups are arranged according to the network rules.

b) M&WPB and Station-Keeping Glider

The glider will produce a large horizontal displacement and the cost of M&WPB is high. We try to observe the performance of the mixed networking of these three types of equipment. The specific strategies are as follows:

Four wave-energy profiling buoy with a mooring were placed as anchor points at the 1st, 7th, 14th, and 20th of the 20 points respectively. The station-keeping gliders were placed in the middle, as shown in Fig. 4(b).

III. RESULT

In order to compare the differences between different in-situ observation networking strategies, we carried out simulation experiments at 20 points as shown in Fig. 1(c) according to the networking methods mentioned above. The influence of different sampling depths on SH reconstruction was verified before the simulation experiment, to determine the rationality of parameter settings of each simulation device. The reconstructed SH array, SSH of the corresponding position, and the difference between them are presented by means of wavenumber spectrum to compare the differences between different sampling strategies. The SWOT baseline error requirement [19] is also introduced as a reference for validation. Should be noted that observation error higher than the baseline does not mean that effective observation cannot be achieved.

A. Vertical Sampling to Different Depths

The vertical velocity of the glider (0.2 m/s) can ensure that data sampling from a 2 km-depth profile to be completed in less than 3 h, which is the temporal resolution of the numerical model. 600 m-depth profile sampling can be completed within 1 h to capture high-frequency signals to the maximum extent. MPB can intensively observe the upper 200 m of the ocean. Moreover, the depth of the experimental sea area is generally more than 4000 m.

Considering the above factors and referring to ROMS depth stratification, we conducted vertical sampling with sampling depths of 200, 600, 2000, and 4000 m in the set point array, respectively. The correlation coefficient between SH and SSH and the root mean square error (RMSD) of their anomalies are shown in Table II, and the results of wavenumber spectrum as shown in Fig. 5.

The wavenumber spectrum of the SH array reconstructed from the temperature-conductivity profile of 2000 m depth is similar to the SH spectrum reconstructed from the 4000 m depth profile. The error-to-signal ratio is almost under 30% at the wavelength

TABLE II
RESULTS OF DIFFERENT DEPTH OBSERVATION

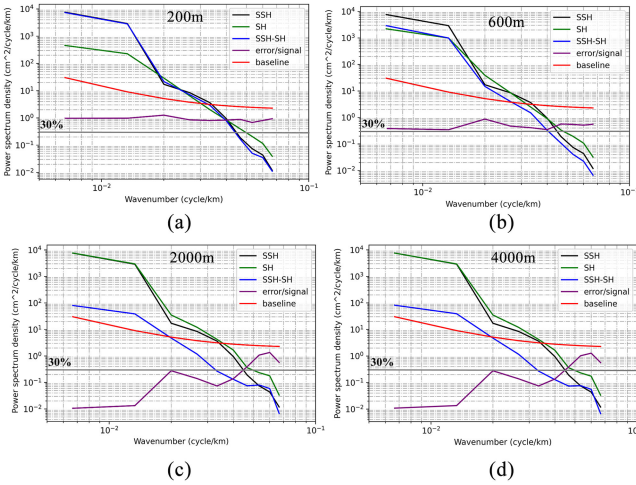| Observation Depth	RMSD(cm)	Correlation Coefficient
200m	14.93	0.6213
600m	8.47	0.9268
2000m	1.89	0.9961
4000m	1.83	0.9960

Fig. 5. Comparison of power spectrum density (PSD) of reconstructed SH (green) of (a) 200 m, (b) 600 m, (c) 2000 m, and (d) 4000 m sampling with SSH (black) and SSH-SH (blue) at set points. Baseline (red) spectrum as a function of wavenumber represented by an empirical function $E(k) = 2 + 0.00125k^{-2}$, where k represents the wavenumber. The error/signal (purple) is the ratio of PSD of SSH-SH and SSH. A visual guide of the 30% (0.3) level (horizontal line).

longer than ∼20 km. The values of PSD of the SSH-SH spectrum are lower as well. However, 600 m profile reconstructed SH spectrum is significantly different from the SSH spectrum, the results of 200 m sampling are also undesirable. The RMSD and correlation coefficient shows the same results. Therefore, it is reasonable to set the sampling depth of each simulation device as 2000 m in this experiment.

It should be noted that the experiments were carried in the high EKE region, and even if the correlation between reconstructed SH and SSH reached more than 99% and the error-to-signal ratio was low, the PSD value was still higher than the SWOT baseline requirements when the wavelengths above 50 km. But at the short wavelength range below 30 km, the PSD of the SSH spectrum lower than the error baseline, and the SH still similar to the SSH spectrum. It means that the in-situ observation can be a good supplement for short-wavelength processes observation.

B. Single-Type Devices Based

The single-type devices array can ensure that the sampling method, the error source, and the degree of being affected by the currents of each sampling point remain unified, and the interference caused by the inconsistency of these influencing factors can be reduced to the greatest extent. In this article, we carried out simulation experiments on arrays with only moorings and only station-keeping gliders.

TABLE III
RESULTS OF DIFFERENT PLATFORMS ARRAYS OBSERVATION IN DIFFERENT STATES

Observation Platforms Array	Affected by Currents or Not	RMSD(cm)	Correlation Coefficient
Mooring	Affected	24.18	-0.2674
	Not Affected	1.42	0.9976
Glider	Affected	1.90	0.9960
	Not Affected	2.19	0.9944
M&WPB	Affected	1.92	0.9962
	Not Affected	1.98	0.9963
Multi-device	Affected	3.04	0.9932
	Not Affected	2.13	0.9962

TABLE IV
ERROR STATISTICS OF DIFFERENT PLATFORMS OBSERVATION

In-situ Observation Platforms	Total Observation Number	the times of the error <2cm	the rate of the error <2cm (%)	the times of the error <5cm	the rate of the error <5cm (%)
Mooring	4800	171	3.6	424	8.8
Glider	5200	2217	42.6	4617	88.8
M&WPB	4800	2044	42.6	4224	88
Multi-device	5200	1898	36.5	4290	82.5

1) Moorings Array: Table III shows the correlation coefficient between SH and SSH and the RMSD of their anomalies. The wavenumber spectrum results of mooring array affected by current and not affected by current are shown in Fig. 6(a) and (b) It can be seen that the SH spectrum reconstructed from the sampled data without the influence of flow velocity (sampling according to the preset position and depth) is relatively consistent with the SSH spectrum of the set point. The SSH-SH spectrum is also significantly lower than the SH spectrum and SSH spectrum when the wavenumber is above 25 km.

However, due to the characteristics of the sea area, the PSD above 50 km wavenumber is higher than the requirement of the baseline. The result of RMSD is 1.42 cm, which is lower than 1.89 cm of the vertical sampling of 2000 m according to the depth stratification of numerical models. It shows that not the denser the sampling is, the more accurate the reconstructed SH is in this area.

The result of sampling influenced by the current is not ideal. By observing the migration results of mooring under the influence of current [as shown in Fig. 6(c)], we found that CTDs migration and sinking are caused by the influence of currents. The upper-ocean data cannot be obtained and the deviation degree of each device in the array is not uniform, the inversion results are greatly different from the real situation. Fig. 6(d) and (e) shows the same results.

2) Gliders Array: Compared with mooring, which is seriously affected by current, although glider has a large horizontal deviation under the influence of current [as shown in Fig. 7(c)], the scatterplot of the anomaly of reconstructed SH, SSH and their difference [as shown in Fig. 7(d) and (e) and Table IV] shows a good consistency, and the wavenumber spectrum results under the influence of current are similar to those results without the influence of current. The RMSD and correlation coefficient
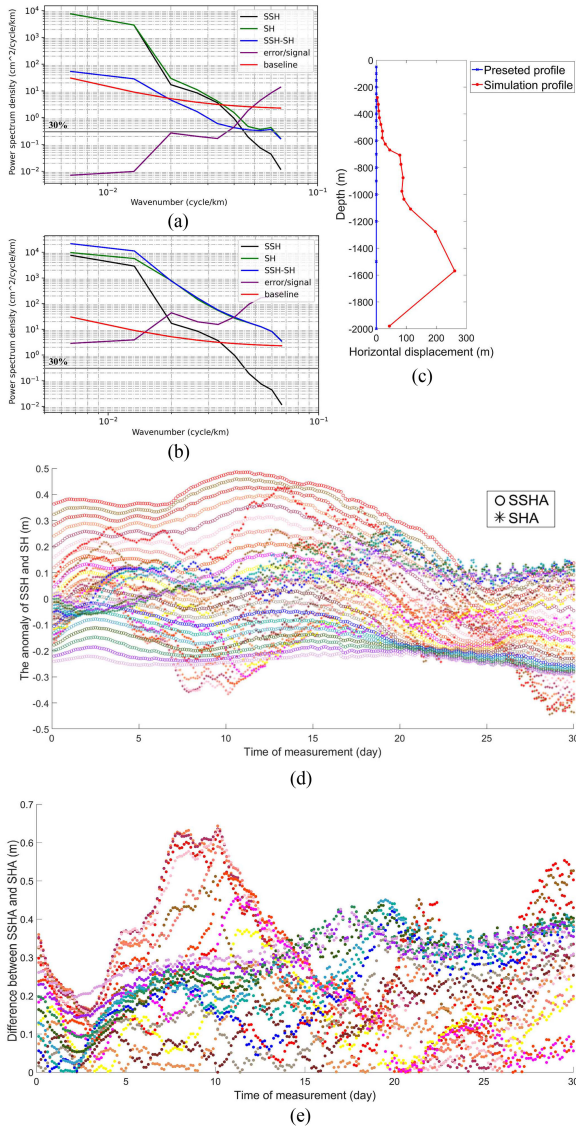
Fig. 6. Wavenumber spectrum of the mooring array that are (a) not affected by current and (b) affected by current. (c) is the comparison of preset profile (blue) and simulation profile (red) of one of the array moorings, the points are the location of CTDs. (d) is the scatterplot of the anomaly of SH and SSH. (e) is the scatterplot of the difference of SHA and SSHA. Twenty different colors represent twenty measurement positions.
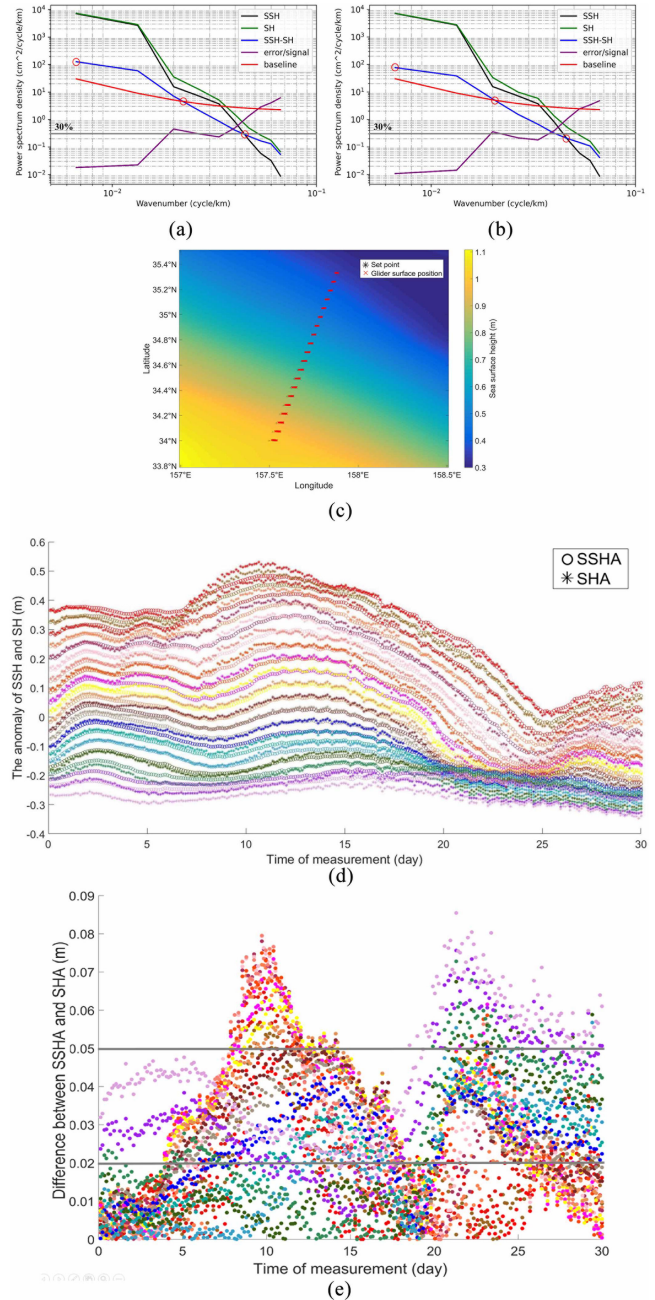

Fig. 7. Wavenumber spectrum of the glider array that are (a) not affected by current and (b) affected by current. The characteristic positions are marked with a red circle. (c) Surface positions of 20 gliders over 30 d, and the base image is SSH of the region. (d) is the scatterplot of the anomaly of SH and SSH. (e) is the scatterplot of the difference of SHA and SSHA. Twenty different colors represent twenty measurement positions. The two gray lines in (e) show errors of 2 and 5 cm, respectively.

affected by currents are better than the results without the influence of currents (as shown in Table III). Comparing the point at 150 km wavenumber of SSH-SH spectrum and the intersection points of SSH-SH spectrum with baseline and SSH spectrum, it was found that glider array had a better effect on the wavenumber scale greater than 50 km (lower PSD of SSH-SH spectrum) under the influence of current, while the vertical sampling results at small scales have better performance.

Similarly, comparing the wavenumber spectrum sampled by glider and mooring without being affected by current, mooring gets better results in the range of large wavenumber and glider gets better results with small scale. This indicates that the higher the spatial sampling frequency is, the better the inversion results will be on the small scale, but it will have an impact on the large scale.

C. Multitype Devices Array

In order to compensate for deviations that may occur in moorings, we connected mooring to WPB that can conduct intensive sampling of the upper ocean. The two kinds of equipment are set as a group at 20 sampling points. Multitype equipment networking can observe the oceanic phenomena with multimode, and the cost of 20 moorings is high. Therefore, we replaced part of the M&WPBs with gliders, as shown in Fig. 4(b).
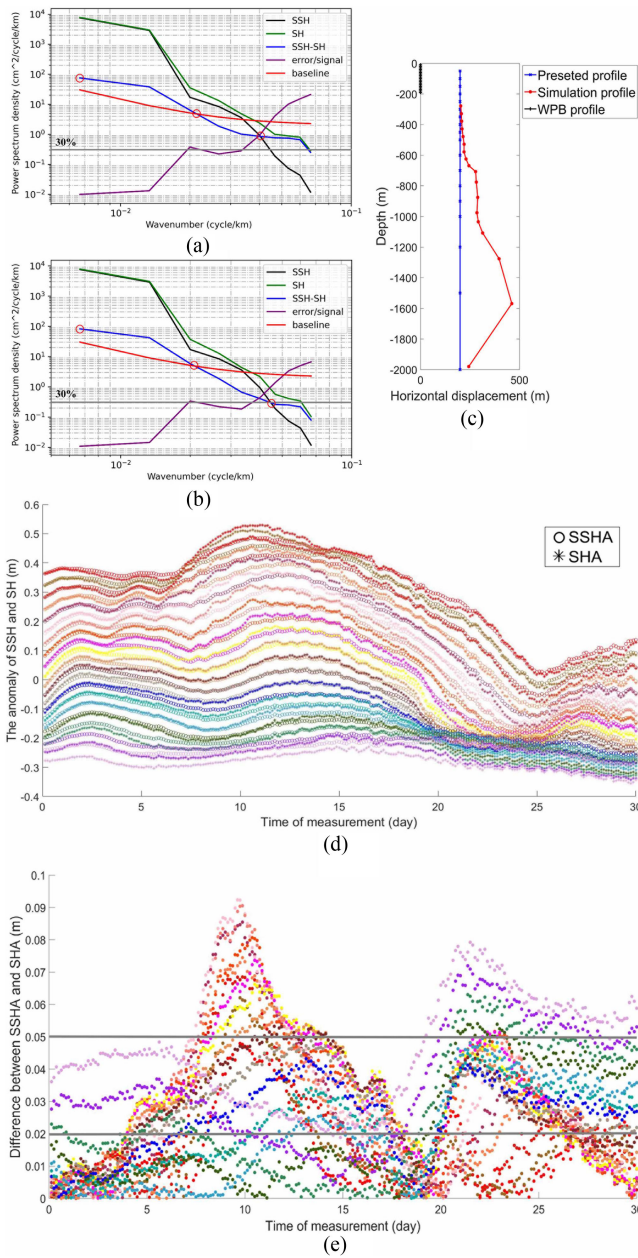
Fig. 8. Wavenumber spectrum of M&WPB array that are (a) not affected by current and (b) affected by current. (c) is the comparison of preset profile (blue) and simulation profile (red) of one mooring of the M&WPB combination array, WPB profile is invariant, and the points is the location of CTDs. (d) is the scatterplot of the anomaly of SH and SSH. (e) is the scatterplot of the difference of SHA and SSHA. Twenty different colors represent twenty measurement positions. The two gray lines in (e) show errors of 2 and 5 cm, respectively.
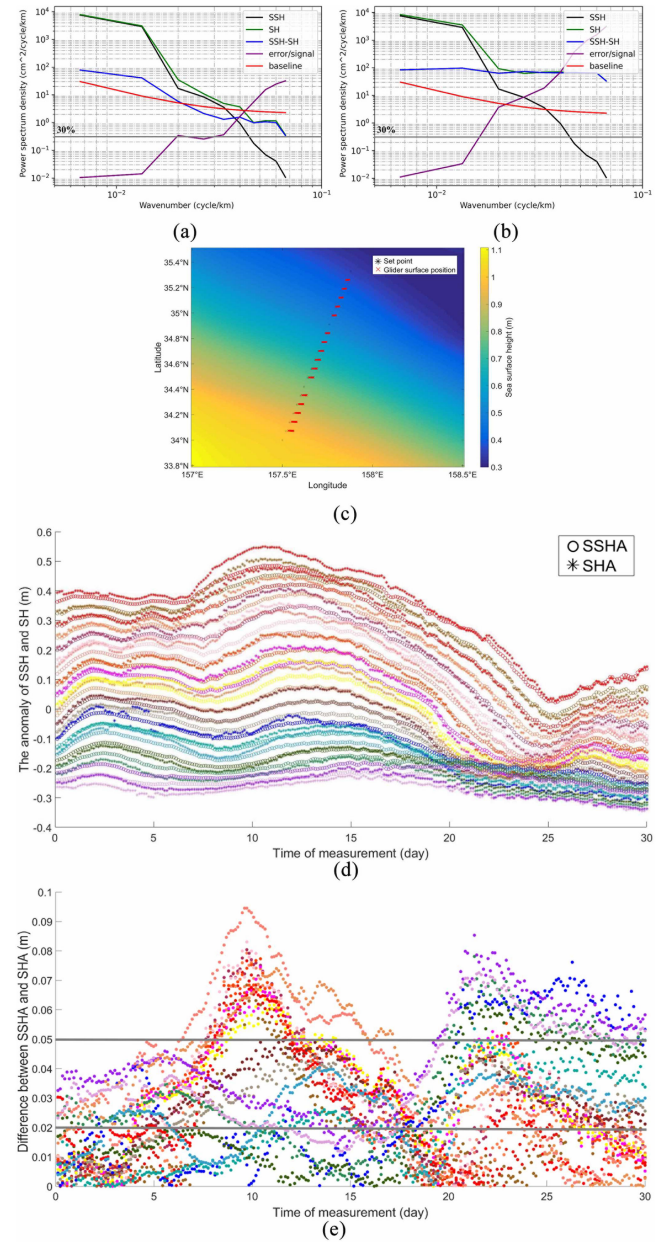

Fig. 9. The wavenumber spectrum of the multiequipment array that not affected by current (a) and affected by current (b). (c) is surface positions of gliders of the array over 30 d, and the base image is SSH of the region. (d) is the scatterplot of the anomaly of SH and SSH. (e) is the scatterplot of the difference of SHA and SSHA. Twenty different colors represent twenty measurement positions. The two gray lines in (e) show errors of 2 and 5 cm, respectively.

1) M&WPBs Array: As shown in Fig. 8(b), (d), and (e) and Tables III and IV, the ability of the M&WPB combination to resist the influence of current is significantly improved compared with that of the mooring array, and the wave-number spectrum results are similar to those of gliders array [Fig. 7(b)]. However, by comparing several characteristic positions, it can be found that the SSH-SH spectrum PSD of the glider array under the influence of current is lower at the wave-number scale of 150 km. The M&WPBs array, which is not affected by current (vertical

sampling), performs worse on small scales. The possible reasons behind that are repeated sampling in the upper ocean by the two devices and inconsistent random errors.

2) Multidevice Array: Compared with the vertical sampling results of the M&WPB combination array [Fig. 8(a), Table III], the SH spectrum [Fig. 9(a)] of the vertical sampling reconstruction of the multidevice array [Fig. 9(a)] fluctuates at small wavenumbers, and the value of RMSD (Table III) is higher, indicating that the inconsistent sampling mode will affect the validation on the 15–25 km scale.

The wavenumber spectrum [Fig. 9(b)] of SH reconstructed from the sampling results under the influence of the current is dominated by error signals (The slope is approximately zero) from the 50-km wavenumbers, the spectrum of 50–100 km wavenumbers is also not consistent enough with the SSH spectrum. The RMSD, which is 3.04 cm, higher than most of the results. The glider surfacing positions of the array [Fig. 9(c)] manifest that station-keeping gliders will have a large horizontal deviation due to the influence of current while the M&WPB combinations have a good station-keeping performance. The disunity of various devices in the array may be the source of errors.

IV. CONCLUSION

The observation of short-wavelength in the high EKE region is difficult and the validation of future WIA 2-D SSH data has always been a challenge. It is therefore the feasibility of using in-situ observation platforms to observe and validate the high EKE region is a problem of exploratory value. We designed a simulation experiment to reveal the differences in observation and validation performance between different in-situ observation platforms array placement strategies and explore the possibility of using in-situ observation equipment to validate ocean phenomena in the WIA swath area through the 15–150 km wavenumber spectrum. Based on the high spatial-temporal resolution numerical model, we introduced the motion model of the mooring and glider trained by the deep learning algorithm under the dynamic ocean current and compared the differences between different observation array strategies.

Due to the influence of strong ocean currents, mooring would have a bias effect, resulting in a blank temperature and salinity data at the upper ocean ($\sim$250 m), and different sampling points would have different degrees of bias due to different flow velocities, leading to high RMSD, low correlation coefficient, and a much higher PSD value of the reconstructed SH array wavenumber spectrum. The M&WPBs array, which uses WPB to observe the upper 200 m of the ocean, could solve this problem.

The station-keeping gliders, which are used as a virtual mooring device, are difficult to maintain within a small horizontal range due to the influence of strong currents. The glider with hybrid power has good anti-current and backtracking ability, and the offset direction and distance of each device in the glider array are correlated due to the characteristics of the current in the experimental area. Startlingly, comparing with the RMSD, correlation coefficient, and the wavenumber spectrum of vertical sampling as the control, the reconstructed SH wavenumber spectrum of glider array affected by currents more consistent with SSH spectrum, and the value of SSH-SH spectrum is lower as well. This indicates that eddy and ocean currents will influence the SH reconstruction.

Due to the inconsistency of sampling mode, movement mode, errors, and other factors of in-situ observation platforms, the performance of a multidevice array is not ideal. This may be because we chose the high EKE region as the experimental region to explore the observation performance of different strategies in the high EKE region. The results might be different in a weak currents region.

Because of the high EKE, none of the observation strategies can achieve that the error spectrum lower than the SWOT error baseline at the wavelength scale greater than 50 km in this simulated experiment. However, the station-keeping gliders array and M&WPBs array are showing good potential for validation and observation. Meanwhile, in-situ observation as a supplement to make up for WIA's inability to capture the dynamic process in the short wavelength range below 30 km in the high EKE region, which could be helpful for the small-scale dynamic process observation.

REFERENCES

[1] R. Ferrari and C. Wunsch, "Ocean circulation kinetic energy: Reservoirs, sources, and sinks," *Annu Rev. Fluid Mech.*, vol. 41, no. 1, pp. 253–282, 2009.

[2] L. Fu *et al.*, "Eddy dynamics from satellite altimetry," *Oceanogr.*, vol. 23, no. 4, pp. 14–25, 2010.

[3] L. Fu and R. Ferrari, "Observing oceanic submesoscale processes from space," *Eos. Trans. Amer. Geophysical Union*, vol. 89, no. 48, pp. 488–488, 2008.

[4] L. Ren *et al.*, "Preliminary evaluation and correction of sea surface height from Chinese Tiangong-2 interferometric imaging radar altimeter," *Remote Sens. Basel*, vol. 12, no. 15, 2020, Art. no. 2496.

[5] R. Morrow *et al.*, "Global observations of fine-scale ocean surface topography with the surface water and ocean topography (SWOT) mission," *Front. Mar. Sci.*, vol. 6, no. 232, pp. 1–19, 2019.

[6] G. Chen *et al.*, "Concept design of the 'Guanlan' science mission: China's novel contribution to space oceanography," *Front. Mar. Sci.*, vol. 6, 2019, Art. no. 194.

[7] C. Ma *et al.*, "An investigation of the influences of SWOT sampling and errors on ocean eddy observation," *Remote Sens. Basel*, vol. 12, no. 17, 2020, Art. no. 2682.

[8] G. D. Quartly *et al.*, "An overview of requirements, procedures and current advances in the calibration/validation of radar altimeters," *Remote Sens. Basel*, vol. 13, no. 1, 2021, Art. no. 125.

[9] S. Sterckx *et al.*, "Towards a European cal/val service for Earth observation," *Int. J. Remote Sens.*, vol. 41, no. 12, pp. 4496–4511, 2020.

[10] T. Dickey *et al.*, "Optical oceanography: Recent advances and future directions using global remote sensing and in situ observations," *Rev. Geophys.*, vol. 44, no. 1, 2006, Art. no. RG1001-n/a.

[11] H. H. Shih, "Recent advances in in-situ ocean observation," in *Proc. ASME 27th Int. Conf. Offshore Mechanics Arctic Eng. vol. 4: Ocean Eng., Offshore Renewable Energy*, Estoril, Portugal, Jun. 2008, pp. 983–994, ASME.

[12] C. Chen, "Retracted: A critical review of internal wave dynamics. Part 1–Remote sensing and in-situ observations," *J. Vib. Control*, vol. 18, no. 3, pp. 417–436, 2011.

[13] P. V. Nagamani *et al.*, "Validation of satellite-derived tropical cyclone heat potential with in situ observations in the North Indian Ocean," *Remote Sens. Lett.*, vol. 3, no. 7, pp. 615–620, 2012.

[14] K. Shitashima, "Integration of in-situ chemical sensors and ocean observing platforms," in *Proc. Techno-Ocean*, 2016, pp. 415–418.

[15] C. Xi *et al.*, "Detailed investigation of the three-dimensional structure of a mesoscale cold eddy in the Kuroshio extension region," *J. Oper. Oceanogr.*, vol. 11, no. 2, pp. 87–99, 2018.

[16] K. A. Donohue *et al.*, "Mapping circulation in the Kuroshio extension with an array of current and pressure recording inverted echo sounders," *J. Atmos. Ocean Tech.*, vol. 27, no. 3, pp. 507–527, 2010.

[17] C. Chupin *et al.*, "Mapping sea surface height using new concepts of kinematic GNSS instruments," *Remote Sens. Basel*, vol. 12, no. 16, 2020, Art. no. 2656.

[18] Q. Zhang *et al.*, "The difference of sea level variability by steric height and altimetry in the North Pacific," *Remote Sens. Basel*, vol. 12, no. 3, 2020, Art. no. 379.

[19] J. Wang *et al.*, "An observing system simulation experiment for the calibration and validation of the surface water ocean topography sea surface height measurement using in situ platforms," *J. Atmos. Ocean Tech.*, vol. 35, no. 2, pp. 281–297, 2018.

[20] T. Xu *et al.*, "Analysis of hydrodynamic behaviors of multiple net cages in combined wave–current flow," *J. Fluid Struct.,* vol. 39, pp. 222–236, 2013.

[21] A. Montano *et al.*, "Numerical simulation of tethered buoy dynamics using mixed finite elements," *Comput. Methods Appl. Mech. Eng.*, vol. 196, no. 41–44, pp. 4117–4129, 2007.

[22] R. K. Dewey, "Mooring design & Dynamics—A MATLAB package for designing and analyzing oceanographic moorings," *Mar. Models*, vol. 1, no. 1, pp. 103–157, 1999.

[23] E. B. Clark *et al.*, "Station-keeping underwater gliders using a predictive ocean circulation model and applications to SWOT calibration and validation," *IEEE J. Ocean. Eng.*, vol. 45, no. 2, pp. 371–384, Apr. 2020.

[24] A. F. Shchepetkin and J. C. McWilliams, "The regional oceanic modeling system (ROMS): A split-explicit, free-surface, topography-following-coordinate oceanic model," *Ocean Model*, vol. 9, no. 4, pp. 347–404, 2005.

[25] P. Yang *et al.*, "On the upper-ocean vertical eddy heat transport in the kuroshio extension. Part I: Variability and dynamics," *J. Phys. Oceanogr.*, vol. 51, no. 1, pp. 229–246, 2021.

[26] S. M. Griffies and R. W. Hallberg, "Biharmonic friction with a Smagorinsky-like viscosity for use in large-scale eddy-permitting ocean models," *Monthly Weather Rev.*, vol. 128, no. 8, pp. 2935–2946, 2000.

[27] W. G. Large *et al.*, "Oceanic vertical mixing: A review and a model with a nonlocal boundary layer parameterization," *Rev. Geophys.*, vol. 32, no. 4, pp. 363–403, 1994.

[28] D. L. Rudnick, "Ocean research enabled by underwater gliders," *Annu. Rev. Mar. Sci.*, vol. 8, no. 1, pp. 519–541, 2016.

[29] D. C. Webb, P. J. Simonetti, and P. J. Jones, "SLOCUM: An underwater glider propelled by environmental energy," *IEEE J. Ocean. Eng.*, vol. 26, no. 4, pp. 447–452, Oct. 2001.

[30] G. M. Damerell *et al.*, "The vertical structure of upper ocean variability at the Porcupine Abyssal plain during 2012–2013," *J. Geophys. Res., Oceans*, vol. 121, no. 5, pp. 3075–3089, 2016.

[31] C. Perigaud, "Influence of interannual rainfall anomalies on sea level variations in the tropical Indian Ocean," *J. Geophysical Res.*, vol. 108, no. C10, 2003, Art. no. 3335.

[32] X. Wang *et al.*, "A probabilistic multimodal optimization algorithm based on Buffon principle and Nyquist sampling theorem for noisy environment," *Appl. Softw. Comput.*, vol. 104, 2021, Art. no. 107068.

Zhiyuan Zhuang was born in Lianyungang, China, in 1997. He received the B.S. degree in geographic information science from the Central South University of Forestry and Technology, Changsha, China, in 2019. He is currently working toward the M.S. degree in cartography and geographic information systems with Ocean University of China, Qingdao, China.

His research interests include marine remote sensing science and technology and ocean data analysis.

Junwu Tang received the B.S. and M.S. degrees in computer science from Tianjin University, Tianjin, China, in 1987 and 1992, respectively, and the Ph.D. degree in remote sensing from the Institute of Remote Sensing Applications, China Academy of Sciences, Beijing, China, in 1999.

He is a General Engineer with the Guanlan Ocean Science Mission, Qingdao National Laboratory for Marine Science and Technology, Qingdao, China. His research interests include ocean optics, ocean color sensing and its Cal/Val, atmospheric correction, and oceanographic LiDAR sensing. He has been working on HY-1 Cal/Val for more than ten years.

Chen Wang was born in Tianjin, China, in 1995. He received the B.S. degree in geography information science from Taiyuan University of Technology, Taiyuan, China, in 2019. He is currently working toward the M.S. degree in cartography and geographic information systems with Ocean University of China, Qingdao, China.

His research interests include calibration and validation of satellite ocean remote sensing and simulation.

Hanwei Sun received the B.S. and Ph.D. degrees from the Beijing Institute of Technology (BIT), Beijing, China, in 2007 and 2012, respectively.

From 2012 to 2014, he was a Postdoctoral Researcher with the Department of Electronic Engineering, Tsinghua University, Beijing, China. He is currently a Senior Engineer with the Beijing Institute of Radio Measurement, Beijing, China. His research interests include imaging altimeter simulation and the design of imaging altimeter airborne/spaceborne systems.

Fangjie Yu received the B.S. degree in electronic information science and technology and the M.S. degree in communication and information system from Shandong University, Jinan, China, in 2002 and 2007, respectively. He is currently working toward the Ph.D. and postdoctorate degree in ocean observation technology, which is based on unmanned mobile platform with Ocean University of China, Qingdao, China, since 2010.

From 2013 to 2016, he was a Postdoctoral Fellow in Marine Technology with Ocean University of China, Qingdao, China. After graduation, he was a Senior R&D Engineer with H3C Ltd., Beijing, China. He is currently an Associate Professor with the Department of Marine Technology, Ocean University of China. His research interests include satellite ocean remote sensing, calibration and validation, and altimeter.

Ge Chen received the M.S. and Ph.D. degrees in marine physics from Ocean University of China, Qingdao, China, in 1990 and 1993, respectively.

He is currently a Professor with the Department of Marine Technology, Ocean University of China, Qingdao, China, and the Chief Scientist with the Engineering Department of "Guanlan" marine science satellite. His research interests include satellite ocean remote sensing, big data oceanography, GIS, and virtual reality technology.